Rupture and afterslip of the 2014 South Napa earthquake reveal spatial variations in fault friction related to lithology

Michael A. Floyd[1], Richard J. Walters[2]*, John R. Elliott[3]†, Gareth J. Funning[4], Jerry L. Svarc[5], Jessica R. Murray[5], Andy J. Hooper[2], Yngvar Larsen[6], Petar Marinkovic[7], Roland Bürgmann[8], Ingrid A. Johanson[8§], and Tim J. Wright[2]

[1]Department of Earth, Atmospheric and Planetary Sciences, Massachusetts Institute of Technology, Cambridge, MA, USA.

[2]COMET, School of Earth and Environment, University of Leeds, Leeds, UK.

[3]COMET, Department of Earth Sciences, University of Oxford, South Parks Road, Oxford, UK.

[4]Department of Earth Sciences, University of California, Riverside, CA, USA.

[5]United States Geological Survey, Menlo Park, CA, USA.

[6]Norut, Tromsø, Norway.

[7]PPO.labs, Den Haag, Netherlands.

[8]Department of Earth and Planetary Science, University of California, Berkeley, CA, USA.

Corresponding author: Michael Floyd (mfloyd@mit.edu)

*Now at: Department of Earth Sciences, Durham University, Elvet Hill, Durham, UK.

†Now at: COMET, School of Earth and Environment, University of Leeds, Leeds, UK.

§Now at: United States Geological Survey, Hawaiian Volcano Observatory, Hawai'i National Park, HI, USA.

Key Points:

- Small-scale spatial and temporal variability of modes of slip observed geodetically
- Afterslip is delimited by variations in lithology more than Coulomb stress changes
- Addition of postseismic contribution increase moment budget by 30%

Abstract

Following earthquakes, faults are often observed to continue slipping aseismically. It has been proposed that this afterslip occurs on parts of the fault with rate-strengthening friction that are stressed by the mainshock, but our understanding has been limited by a lack of immediate, high-resolution observations. Here we show that the behavior of afterslip following the 2014 South Napa earthquake varied over distances of only a few kilometers. This variability cannot be explained by coseismic stress changes alone. We present daily positions from continuous and survey GPS sites that we re-measured within 12 hours of the mainshock, and surface displacements from the new Sentinel-1 radar mission. This unique geodetic data set constrains the distribution and evolution of coseismic and postseismic fault slip with exceptional resolution in space and time. We suggest that the observed heterogeneity in behavior is caused by lithological controls on the frictional properties of the fault plane.

1 Introduction

The South Napa earthquake (M_w6.1, 24 August 2014, 10:20 UTC) was the largest earthquake in the San Francisco Bay Area since 1989. It produced a 12 km-long surface rupture with right-lateral strike-slip displacement, as well as multiple sub-parallel secondary ruptures to the east [*GEER Association*, 2015; *Hudnut et al.*, 2014; *Morelan et al.*, 2015]. Although most of the ruptured segments had been mapped prior to the earthquake [*Fox et al.*, 1973; *Wesling and Hanson*, 2008], it was not clearly recognized how active these strands of the West Napa Fault (WNF) system were, what magnitude of earthquake they may be capable of producing, or how they may interact with one another during such an event. On the morning of August 24, crews tasked with the repair of Highway 12, whose surface was broken and offset by the coseismic rupture, noted that the slip on the fault continued to grow [*GEER Association*, 2015; *Morelan et al.*, 2015]. Mapping during the days that followed confirmed similar behavior along most of the main surface rupture [*GEER Association*, 2015]. In some places this "afterslip" exceeded the coseismic slip [*Hudnut et al.*, 2014; *Lienkaemper et al.*, 2016].

Many moderate-to-large earthquakes are followed by slow postseismic slip on the causative fault or neighboring structures [*Wright et al.*, 2013], which modifies fault stress and therefore also affects the distribution of aftershocks and seismic hazard. This aseismic slip is thought to be driven by coseismic static stress changes (producing afterslip) or dynamic stress changes ("triggered slip") acting on parts of the fault with rate-strengthening friction and therefore provides an opportunity to infer variations in frictional properties [*Scholz*, 1998]. Along-strike differences (and episodicity) of surface creep on some faults [e.g. *Lienkaemper et al.*, 2001] has previously hinted at such variations, but current observations lack resolving power at depth. Previous studies of the South Napa earthquake have concluded that additional near-field geodetic observations of coseismic and postseismic deformation are key to defining such details of the properties of the shallow fault zone [*Wei et al.*, 2015], which, in turn, are vital to understanding the physical mechanisms driving the afterslip.

We have compiled a geodetic dataset with exceptional spatial and temporal resolution to achieve these aims. Within 12 hours of the mainshock, we re-measured a dense network of survey-mode GPS sites surrounding the WNF and recorded their positions continuously for a further three weeks, supplementing a sparser, regional-scale, continuously-operating GPS network. The earthquake was also the first significant earthquake to be imaged by the radar satellite Sentinel-1A, whose 12-day imaging repeat interval and tight orbital control enable us to map surface displacements with fine spatial resolution and minimal decorrelation [*Elliott et*

al., 2015]. The combination of these complementary data sets (see Supporting Information) allows us to resolve the distribution in space and evolution in time of postseismic fault slip across the WNF system, and its relationship with the coseismic slip.

Modeling these geodetic data reveals a highly variable spatiotemporal pattern of slip, during and following the 2014 South Napa earthquake, both at the surface and at depth. These observations cannot be simply explained by the response of a fault with uniform frictional properties to the coseismic stress changes. Furthermore, this fault was not previously observed to exhibit creep behavior yet underwent significant aseismic afterslip, increasing the total moment released as a result of the earthquake, and posing an additional infrastructure hazard for a period of several weeks [*Lienkaemper et al.*, 2016]. This prompts a re-evaluation of the nature of historical earthquakes and characteristics applied to all faults, both creeping and non-creeping, when used in probabilistic seismic hazard analyses [*EERI*, 2014].

2 Geodetic Data

2.1 Survey and continuous GPS

The South Napa earthquake occurred in an area in which survey GPS network coverage is denser than that from continuous GPS sites; there are only six continuous sites within 25 km of the surface rupture. Continuous GPS sites in the region belong to the Bay Area Regional Deformation (BARD; http://seismo.berkeley.edu/bard/) and Plate Boundary Observatory (PBO; http://www.unavco.org/projects/major-projects/pbo/pbo.html) networks. The survey sites, providing denser observations at closer proximity to the rupture, were previously established by the U. S. Geological Survey (USGS; http://earthquake.usgs.gov/monitoring/gps/NCalifornia_SGPS/) and California Spatial Reference Center (http://csrc.ucsd.edu/projects/norcal2004.html and http://csrc.ucsd.edu/cenchm2007.shtml), and measured by the University of California, Riverside (UCR) and the Massachusetts Institute of Technology (MIT) in intervening years. Two groups, one from UCR and MIT, and one from the USGS, responded quickly to the earthquake, occupying 26 survey GPS sites between them within 48 hours, including nine UCR-MIT sites that were measured within 15 hours of the mainshock. Fortuitously, many of the UCR-MIT sites had been surveyed just seven weeks before the earthquake, yielding precise pre-event positions that, in turn, produced precise estimates of coseismic displacement (Figure 1a and Table S1). To capture the initial post earthquake motions, 24 of the survey GPS sites were observed continuously for between 7 and 25 days after the earthquake.

GPS data were processed in daily, 24-hour sessions using the GAMIT/GLOBK (version 10.5) software suite [*Herring et al.*, 2015]. Raw GPS phase data from before, during and after the earthquake at all sites within the region with available data were processed using IGS final orbits, IERS Bulletin B Earth orientation parameters [*Petit and Luzum*, 2010], FES2004 ocean tide loading model [*Lyard et al.*, 2006] and the empirical GPT2 a priori zenith delay and mapping functions [*Lagler et al.*, 2013]. Time series were produced from the daily solutions and logarithmic fits to the postseismic data [*Marone et al.*, 1991] were estimated by linearized least-squares adjustments using partial derivatives: The post-earthquake GPS time series are expressed relative to the site's estimated pre-earthquake velocity and fit using a natural logarithmic decay function of the form $x(t) = x_0 + a \ln(dt/\tau + 1)$, where x_0 is an initial position, a is the amplitude of the logarithm, dt is the time since the earthquake and τ is the decay time constant. The decay time constant for sites closest to the rupture (e.g. DEAL, 04LG, TRAN, B468) is less than 1 day, with horizontal amplitudes up to

35 mm. Time series from proximal continuous GPS sites are analysed to estimate time correlated noise using the algorithm described by *Herring* [2003] and *Reilinger et al.* [2006]. A final solution was then produced using a Kalman filter to combine all pre-, co- and post-earthquake data, during which coseismic offsets were estimated at the epoch of the earthquake, accounting for the postseismic decay terms previously estimated in the a priori coordinate model. Temporally correlated noise is also included in the Kalman filter by means of an equivalent random walk to recreate long-term uncertainties. A selection of post-earthquake time series from ten GPS sites close to the epicenter that show significant coseismic displacements is shown in Figure S1.

In total, 49 GPS sites show significant (at the one-sigma level) coseismic displacements (Figure 1a, Table S1). Maximum surface displacements of approximately 20 cm are seen at three survey GPS sites within 3 km of the surface rupture. Following the mainshock, our postseismic GPS time series (Figure S1) show continued surface displacement with broadly similar directions, consistent with the occurrence of afterslip. Differences in azimuth in between the coseismic and postseismic displacements at individual sites show that the distribution of afterslip differs from that of the coseismic slip (compare Figure 1a to Figure S3). The GPS dataset we present here is much more complete, especially in the near-field (< 15 km from the rupture), than that presented in previous studies for this earthquake [*Barnhart et al.*, 2015; *Dreger et al.*, 2015; *Wei et al.*, 2015; *Melgar et al.*, 2015].
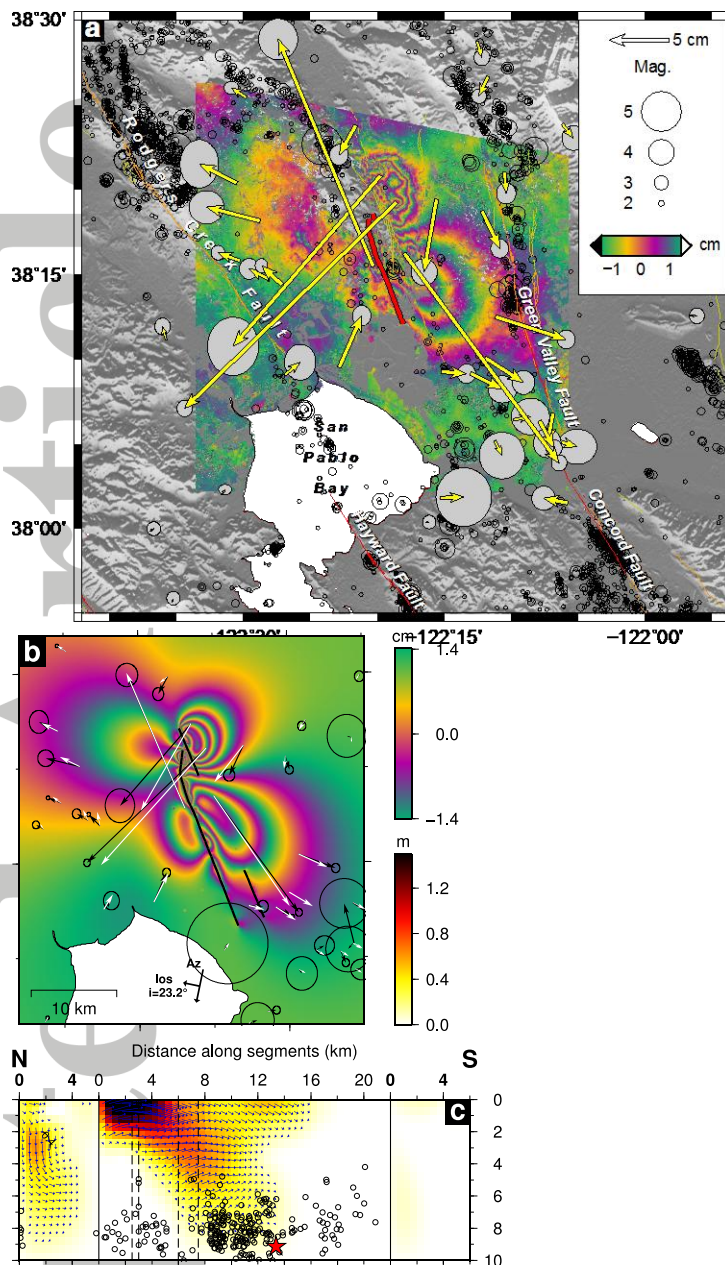
Figure 1. Summary of coseismic geodetic data and model for the 2014-08-24 South Napa earthquake. **a** Tectonic map of the epicentral region showing pre-earthquake seismicity [*Waldhauser*, 2009] (black circles), mapped surface rupture of the South Napa earthquake [*Morelan et al.*, 2015] (thick red line), horizontal coseismic GPS displacements (yellow vectors) with 95% confidence ellipses, and line-of-sight InSAR displacements (color map); **b** Result of data inversion showing the model faults used (black lines), GPS displacement data (black vectors), predicted GPS displacements (white vectors) and predicted InSAR; **c** View of the modeled coseismic slip on the fault plane. Solid vertical lines delineate the separate (from left to right) northern step-over segment, main segment and southeastern Napa airport segment; dashed vertical lines represent changes in strike along the main segment, as shown in (b). The hypocenter is marked by the red star and aftershocks by black circles. Contours of coseismic slip are at 0.4 m intervals.

2.2 Sentinel-1A InSAR

We processed Sentinel-1A Stripmap SAR data from raw products, correcting the resulting interferograms for orbital effects using orbits from the European Space Agency, and for topographic effects using 3-arcsecond SRTM digital topography. Atmospheric effects that correlated with topography in the postseismic interferograms were mitigated by removing a best-fit linear function of phase versus elevation, using a 15 m LiDAR DEM. We downsampled the InSAR data before modeling using nested uniform sampling with a resolution of 1.8 km in the far field and 200 m in the near field. We present six Sentinel-1 interferograms, one spanning the earthquake and five post-earthquake intervals up until the end of November 2014. The Sentinel-1A SAR satellite, which launched just four months prior to the earthquake, provides data acquisitions at regular 12-day intervals enable a time series of cumulative ground deformation to be calculated from the set of interferograms. The coseismic interferogram (2014-08-07 to 2014-08-31, which includes seven days of postseismic motion) is shown in Figure 1a and cumulative line-of-sight displacements over five post-earthquake intervals are shown in Figure 2.

3 Combined coseismic slip and afterslip modeling

Using both the GPS and InSAR data, we solve for the temporal evolution of the distribution of slip on the WNF, in the coseismic and postseismic periods, in a single inversion process using a modified version of the *slipinv* code [*Funning et al.*, 2005] (see Figure S2). We solve for incremental slip during 13 time steps: the coseismic slip interval, each of the first seven days after the earthquake (and before the first post-earthquake SAR acquisition), then the five 12-day intervals between subsequent SAR acquisitions. Coseismic slip is constrained by the estimates of coseismic displacement from GPS (see Section 2.1) whilst the first InSAR interferogram (Figure 1a) constrains the sum of the coseismic slip and the first seven days of postseismic slip. In the post-seismic period, the displacement over each time increment is constrained by GPS and InSAR data. InSAR data are down-weighted by a factor of 5 relative to the GPS, to take account of the higher uncertainties on the InSAR data and larger number of measurements. Spatial smoothing is applied to the slip distributions by using a Laplacian operator [*Harris and Segall*, 1987], and a positivity constraint is also applied, but no temporal smoothing is implemented. Rake is allowed to vary across the fault plane for the coseismic interval, but is fixed for the postseismic increments to the average coseismic rake for each segment. A detailed description of our approach to constrain the model fault geometry is in the Supporting Information (Text S1).

Our model of coseismic slip (Figure 1c) shows that the majority of moment release occurred at shallow depths, less than 5 km below the surface, and extending 15 km north of the epicenter. The peak slip is 1.6 m, located at a depth of ~1 km just south of the bend in the main fault trace, in the region where the greatest surface offsets of 46 cm were recorded [*Hudnut et al.*, 2014; *Morelan et al.*, 2015; *Lienkaemper et al.*, 2016; *Wei et al.*, 2015]. We also find surface displacements of ~ 25 cm further south, in agreement with field mapping [*Hudnut et al.*, 2014; *Morelan et al.*, 2015]. Significant slip occurred at depth between the main patch of slip and the hypocenter (red star in Figure 1c) and on the stepover segment to the north. The seismic moment of 1.67×10^{18} N m ($M_w6.1$) is consistent with purely seismological estimates [*Dreger et al.*, 2015] and models that also incorporate geodetic data [*Dreger et al.*, 2015; *Barnhart et al.*, 2015], suggesting that any afterslip occurring in the few hours before the survey GPS deployment did not contribute significantly to the total moment release.

4 Postseismic slip results

Our models of postseismic slip over each time interval (Figure 2b-f, Figures S3 and S4) reveal several key features. Very shallow afterslip occurs above and to the south of the coseismic slip at an initially steady rate of several cm per day and persists over at least the first four weeks after the earthquake (e.g. green time series and boxes in Figure 3). Shallow afterslip also occurs north of the northern end of the main rupture, and deepens and increases in magnitude approximately three weeks after the earthquake (Figure 2c-f, blue time series and boxes in Figure 3). This deep slip does not appear to decay over the time period of our observations. Triggered slip is also apparent away from the main rupture. Surface offsets were observed at Napa Airport on a sub-parallel fault strand approximately 3 km to the east of the southern end of the main rupture and our model shows deeper afterslip, further to the south on this segment. The displacement time series at continuous GPS site P261, about 9 km south-east of the epicenter, is consistent with this deep triggered slip to the south continuing six months after the earthquake (Figure S2). Given the limited GPS coverage and InSAR coherence in this area, due to coastal marshland and San Pablo Bay, we cannot rule out that aseismic slip continues further south still. The two apparent deep postseismic slip patches modeled in the first 3 days are unlikely to be real, as they have high associated uncertainties and occur in regions with poor resolution (Figures S4 and S5), but all the other features described previously are robustly resolved.
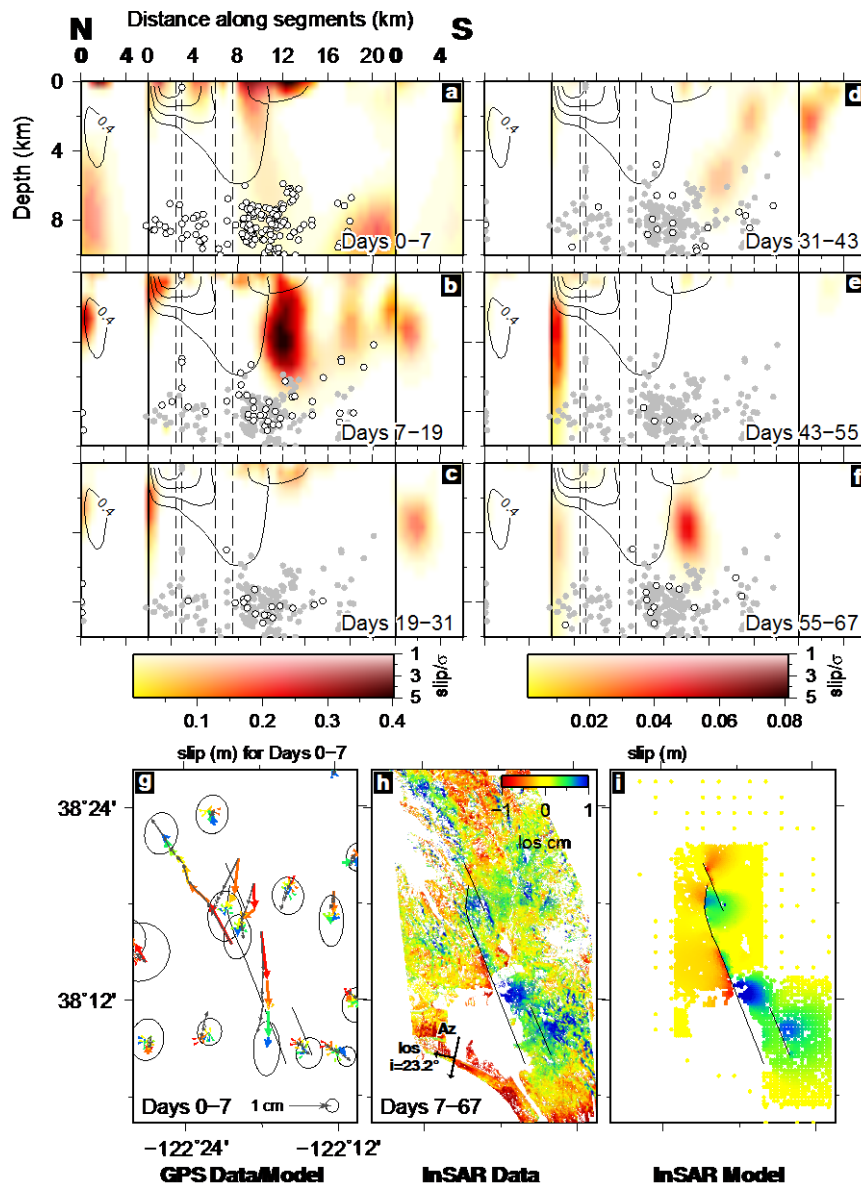
Figure 2. Fault afterslip distributions, and cumulative geodetic data and model. **a**, **b**, **c**, **d**, **e**, **f** Incremental slip distributions on the model fault plane over the annotated intervals. Higher confidence (ratio of slip magnitude-to-uncertainty) estimates are represented by darker color saturations. Black contour lines on each panel represent the coseismic slip shown in Figure 1c, whilst the dots show aftershock locations, projected orthogonally onto the fault plane, during (white) and before (gray) the current time interval. Solid vertical lines delineate the step-over segment (north), main segment (center) and Napa airport segment (south), and dashed vertical lines represent changes in strike on the main segment, as in Figure 1c. **g** Cumulative GPS displacements for the first seven days following the earthquake are shown by colored vectors (red for displacement on day 1 through to blue for displacement on day 7 after the earthquake), with ellipses showing one-sigma uncertainties on the cumulative displacement. Gray arrows show the model fit to the data. **h**, **i** Cumulative InSAR line-of-sight displacement data for days 7–67 following the earthquake (**h**), and modeled displacements displayed for downsampled data points only (see Section 2.1) (**i**). The black lines show the surface trace of the model fault.

In total, we estimate postseismic moment release during the first 67 days to be 0.50×10^{18} N m, approximately 30% of the coseismic moment and equivalent to a $M_w 5.7$ earthquake. Aftershocks occur mostly in a deep zone (7 km depth and greater) located south of the main coseismic slip zone (white and gray dots in Figure 2a-f; pink dots in Figure 3). The area directly beneath the coseismic rupture but above the zone of aftershocks, marked with a black cross in Figure 3d, has little afterslip, as resolved by the current geodetic observations. This likely unruptured segment of the fault, perhaps reflecting local structural controls that discourage seismic rupture or aseismic afterslip, may represent a continuing seismic hazard [*Elliott et al.*, 2013; *Elliott et al.*, 2011].

5 Discussion

The widespread and rapid afterslip along the WNF posed an infrastructure hazard in its own right. Repeated repairs of major roads cross-cut by the rupture were required and, in some areas, water pipes that survived the coseismic offset were subsequently broken by the afterslip [*GEER Association*, 2015]. Coulomb stress changes on the West Napa Fault are consistent with several of the areas of afterslip and triggered aftershocks [*Stein*, 1999]. For example, the persistent and deepening afterslip described above (i.e. blue time series and boxes in Figure 3) appears in a region of reduced normal stress near the fault's releasing step-over (Figure S6). Such stress-driven afterslip in a rate-and-state friction framework was inferred by *Wei et al.* [2015] to be compatible with the post-earthquake GPS and alignment array data available to them, although they present a forward model and do not directly invert the geodetic data for afterslip on the fault plane as we present here. The shallow regions of afterslip may be adequately modeled as the response of a rate-strengthening fault surface in the uppermost $1–1.5$ km to changes in shear stress associated with the mainshock [*Marone et al.*, 1991; *Wei et al.*, 2015]. However, we find that stress changes alone cannot fully explain the wide variety of afterslip behaviors in our models or their evolution with time (Figure 3). The short-scale variability of coseismic slip and afterslip shown by inversion of our geodetic data, to which both the GPS and InSAR contributions are of higher density in space and time, may suggest that constitutive parameters associated with rate-and-state friction models vary over distances of just a few kilometers. We therefore propose that variations in subsurface lithology play an important role in determining both the coseismic slip pattern, and loci and evolution of postseismic processes following the earthquake.

Geologic mapping of the Napa Valley area suggests large lithologic strength contrasts across the WNF and with depth. To the west lie the Mayacamas Mountains, a basement ridge whose eastern flank is composed of late Mesozoic and early Tertiary sequences [*Graymer et al.*, 2007]. To the east, the center of Napa Valley is dominated by surficial Quaternary alluvial deposits. Moving southwards along the main rupture, gravity data and seismic velocity models suggest increasing thicknesses of these unconsolidated sediments, from 1.5 km in the north to 2 km in the south, as the Napa River delta meets San Pablo Bay [*Langenheim et al.*, 2010]. There is a clear spatial correlation between surface lithology and mode of slip during and following the 2014 South Napa earthquake (Figure 4). The main coseismic slip regions occurred where the WNF is adjacent to the Franciscan basement rocks. In addition, the region of triggered slip occurred on a section of the south-eastern fault segment that also lies against this unit. However, this coseismic slip dies out into the younger Cenozoic sediments and Quaternary alluvium, and
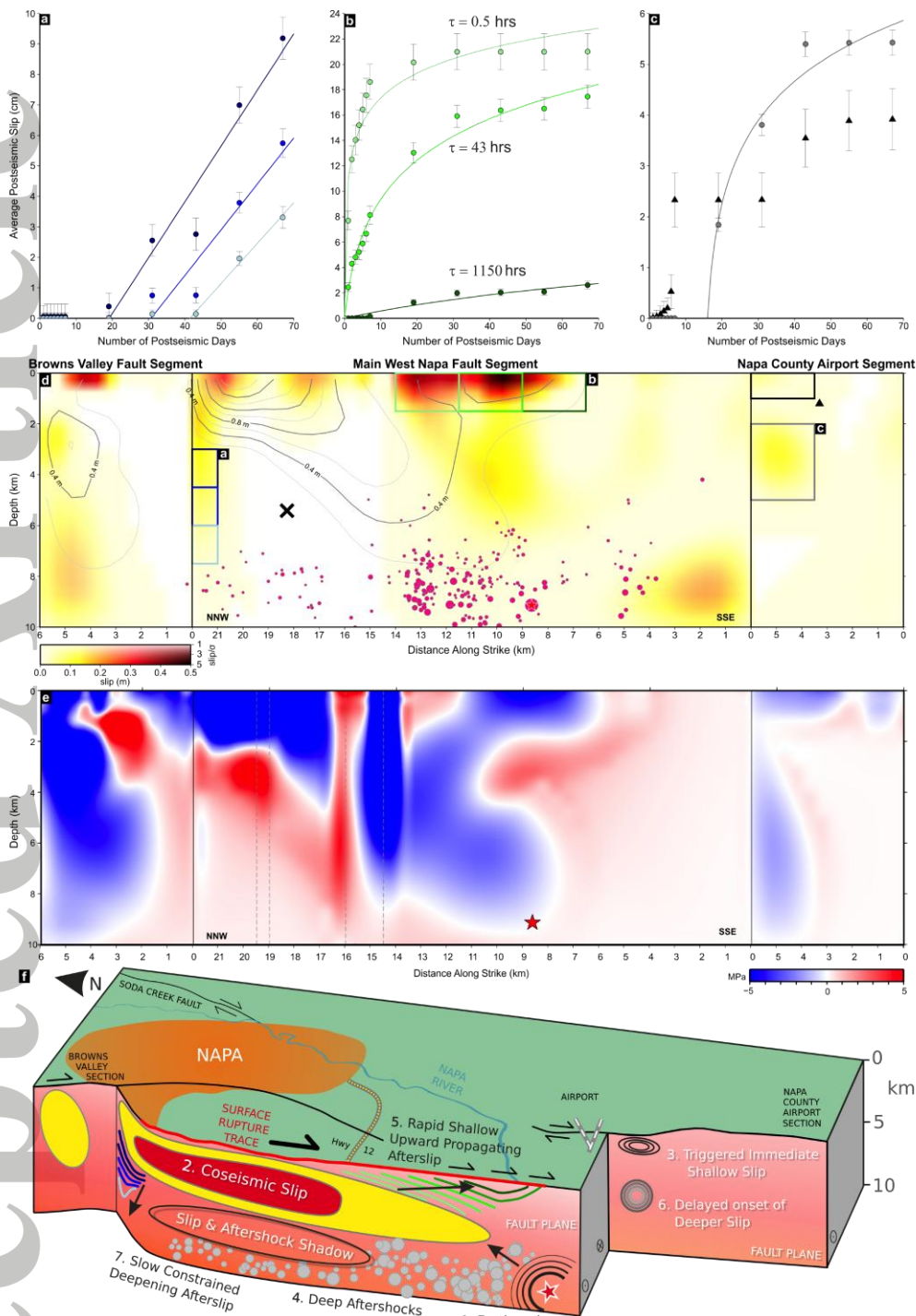
Figure 3. Variable behavior in time and space of afterslip, and relationship of cumulative slip to coseismic Coulomb stress changes and aftershocks. **a**, **b**, **c** Temporal evolution of characteristic slip on patches of the fault. **d** Cumulative slip distribution across the model fault plane, where colored boxes correspond to the patches shown in the slip evolution time series, above. Segmentation of the model fault is as in Figures 1c and 2. **e** Coulomb stress change on the West Napa Fault plane due to modeled coseismic slip distribution (see Figure 1c). **f** Schematic summary of our findings, as described in the text, showing the sequence of slip behavior.

afterslip (both shallow and deepening) occurs around the coseismic regions in both these lithological units. This is supported by geologic cross-sections [e.g. *Wagner and Bortugno*,

1982], which also show Sonomo volcanics contacting Cenozoic sediments in the upper 0.5 km where the major afterslip is concentrated. This clear relationship between mode of slip and lithology implies that lithology is exerting a significant control on fault frictional properties over short (several km) distances. Such short-scale contrasts in the timing of onset and rate of afterslip may be due to heterogeneities in clay content or mineralogy, or pore pressure variations within the sediments.
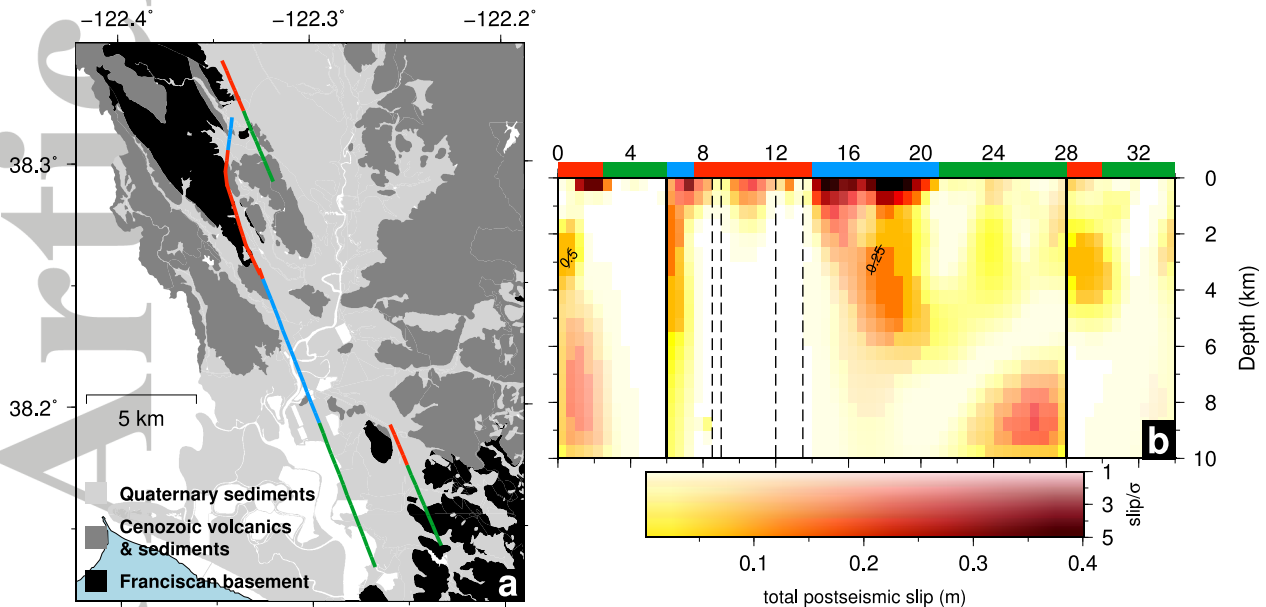

Figure 4. Spatial relationship between the major types of lithological units and the co- and post-seismic slip patterns during the 2014 earthquake. **a** Along-strike variations of slip type, shown as fault segments colored red (predominant coseismic slip or triggered slip), blue (major afterslip), or green (minor or insignificant coseismic or postseismic slip). The background, adapted from the geological map of Napa County from *Graymer et al.* [2006, 2007] and references therein, shows the distribution of the major geologic units: black represents Cretaceous basement rocks from the Franciscan Complex, mostly the Great Valley Sequence; dark gray represents consolidated Cenozoic volcanic and sedimentary rocks, including Sonoma Volcanics; light gray represents Quaternary alluvial deposits. **b** Corresponding slip, as modeled in this study. Color shows total afterslip to day 67, contours show coseismic slip. Panel is the same as in Figures 1c, 2a-f and 3b. Red, blue and green lines demark the same along-strike variations as described for (a).

6 Conclusions and implications

We have identified multiple distinct areas on the fault surface that show differing amounts of coseismic and postseismic slip, derived from a full inversion of complete near- and far-field GPS data set in combination with the first Sentinel-1A InSAR data, as well as differing aftershock activity. We attribute the clear division between the zones dominated by slip in the earthquake and those which mostly slipped after it to a likely difference in the WNF's frictional properties, from rate-weakening (which favors propagation of seismic rupture) to rate-strengthening (which arrests earthquake slip and promotes slow sliding), respectively. These differences in slip timing and behavior on different portions of the fault, and therefore their likely frictional properties, may correlate with surface geology. In addition, the differences in the amounts of slip, and their temporal evolution, between different portions of the fault undergoing afterslip, suggest variations in frictional constitutive

parameters on the fault surface that manifest over distances of only a few kilometers, which may themselves reflect lithological features in the fault zone. No aftershocks are observed in relation to the shallow (< 2 km depth) afterslip, suggesting that the conditions there do not promote seismic failure.

These observations have implications for our understanding of how shallow slip contributes to the earthquake cycle aseismically rather than in seismic rupture, as implicitly assumed by paleoseismological estimates of earthquake slip magnitude. Current probabilistic seismic hazard analyses take into account "aseismic factors" [*Field et al.*, 2013], which represent the ratio of long-term creep rate to total slip rate. However, here a fault that has a low slip rate (< 4 mm/yr) [*d'Alessio et al.*, 2005; *Wesling and Hanson*, 2008] and was not previously known to creep aseismically is shown to exhibit significant heterogeneous shallow afterslip in the aftermath of a large earthquake. We suggest that varying frictional regimes over scales of just a few kilometers, possibly related to local geological variations, play an as-yet unaccounted for but significant role in models of fault mechanics and should influence seismic hazard assessments.

Acknowledgments and Data

References

Aagaard, B. T., R. W. Graves, A. Rodgers, T. M. Brocher, R. W. Simpson, D. Dreger, N. A. Petersson, S. C. Larsen, S. Ma, and R. C. Jachens (2010), Ground-motion modeling of 199 Hayward Fault scenario earthquakes, part II: simulation of long-period and broadband ground motions, Bull. Seismol. Soc. Amer., 100, 2945–2977, doi:10.1785/0120090379.

Avouac, J.-P. (2015), From geodetic imaging of seismic and aseismic fault slip to dynamic modeling of the seismic cycle, Annu. Rev. Earth Planet. Sci., 43, 233–271, doi: 10.1146/annurev-earth-060614-105302.

Barnhart, W. D., J. R. Murray, S.-H. Yun, J. L. Svarc, S. V. Samsonov, E. J. Fielding, B. A. Brooks, and P. Milillo (2015), Geodetic constraints on the 2014 M 6.0 South Napa earthquake, Seismol. Res. Lett., 86, 335–343, doi:10.1785/0220140210.

California Earthquake Clearinghouse (2014), M 6.0 South Napa earthquake of August 24, 2014, Earthquake Engineering Research Institute Special Earthquake Report, http://www.eqclearinghouse.org/2014-08-24-south-napa/preliminary-reports/#eerireport.

d'Alessio, M. A., I. A. Johanson, R. Bürgmann, D. A. Schmidt, and M. H. Murray (2005), Slicing up the San Francisco Bay Area: block kinematics and fault slip rates from GPS derived surface velocities, J. Geophys. Res., 110, B06403, doi: 10.1029/2004JB003496.

Dreger, D. S., M.-H. Huang, A. Rodgers, T. Taira, and K. Wooddell (2015), Kinematic finite source model for the 24 August 2014 South Napa, California, earthquake from joint inversion of seismic, GPS, and InSAR data, Seismol. Res. Lett., 86, 327–334, doi:10.1785/0220140244.

Elliott, J. R., B. Parsons, J. A. Jackson, X. Shan, R. A. Sloan, and R. T. Walker (2011), Depth segmentation of the seismogenic continental crust: The 2008 and 2009 Qaidam earthquakes, Geophys. Res. Lett., 38, L06305, doi:10.1029/2011GL046897.

Elliott, J. R., A. C. Copley, R. Holley, K. Scharer, and B. Parsons (2013), The 2011 Mw 7.1 Van (eastern Turkey) earthquake. J. Geophys. Res., 118, 1619–1637, doi:10.1002/jgrb.50117.

Elliott, J. R., A. J. Elliott, A. Hooper, Y. Larsen, P. Marinkovic, and T. J. Wright (2015), Earthquake Monitoring Gets Boost from New Satellite, Eos, 96, doi:10.1029/2015EO023967.

Field, E. H., G. P. Biasi, P. Bird, T. E. Dawson, K. R. Felzer, D. D. Jackson, K. M. Johnson, T. H. Jordan, C. Madden, A. J. Michael, K. R. Milner, M. T. Page, T. Parsons, P. M. Powers, B. E. Shaw, W. R. Thatcher, R. J. Weldon II, and Y. Zeng (2013), The Uniform California Earthquake Rupture Forecast, version 3 (UCERF3)—the time-independent model. USGS Open-File Report 2013–1165, CGS Special Report 228, Southern California Earthquake Center Publication 1792, http://pubs.usgs.gov/of/2013/1165/.

Fox, K.F., J. D. Sims, J. A. Bartow, and E. J. Helley (1973), Preliminary geologic map of eastern Sonoma County and western Napa County, California, Miscellaneous Field Studies Map MF-483, U.S. Geological Survey, http://ngmdb.usgs.gov/Prodesc/proddesc_279.htm.

Funning, G. J., B. Parsons, T. J. Wright, J. A. Jackson, and E. J. Fielding (2005), Surface displacements and source parameters of the 2003 Bam (Iran) earthquake from Envisat advanced synthetic aperture radar imagery, J. Geophys. Res., 110, B09406, doi:10.1029/2004JB003338.

Geotechnical Extreme Events Reconnaissance (GEER) Association (2015), Geotechnical engineering reconnaissance of the August 24, 2014 M6 South Napa, GEER Association Report No. GEER-037,

http://www.geerassociation.org/GEER_Post%20EQ%20Reports/SouthNapa_2014/index.html.

Graymer, R. W., B. C. Moring, G. J. Saucedo, C. M. Wentworth, E. E. Brabb, and K. L. Knudsen (2006), Geologic Map of the San Francisco Bay Region, U.S. Geological Survey, Scientific Investigations Map 2918, http://pubs.usgs.gov/sim/2006/2918/.

Graymer, R. W., E. E. Brabb, D. L. Jones, J. Barnes, R. S. Nicholson, and R. E. Stamski (2007), Geologic map and map database of eastern Sonoma and western Napa Counties, California, U.S. Geological Survey, Scientific Investigations Map 2956, http://pubs.usgs.gov/sim/2007/2956/.

Harris, R. A., and P. Segall (1987), Detection of a locked zone at depth on the Parkfield, California, segment of the San Andreas Fault, J. Geophys. Res., 92, 7945–7962, doi:10.1029/JB092iB08p07945.

Herring, T. (2003), MATLAB Tools for viewing GPS velocities and time series, GPS Solut., 7, 194–199, doi:10.1007/s10291-003-0068-0.

Herring, T. A., R. W. King, M. A. Floyd, and S. C. McClusky (2015), Introduction to GAMIT/GLOBK, Release 10.6, http://www-gpsg.mit.edu/~simon/gtgk/Intro_GG.pdf.

Hudnut, K. W., T. M. Brocher, C. S. Prentice, J. Boatwright, B. A. Brooks, B. T. Aagaard, J. L. Blair, J. B. Fletcher, J. E. Erdem, C. W. Wicks, J. R. Murray, F. F. Pollitz, J. Langbein, J. Svarc, D. P. Schwartz, D. J. Ponti, S. Hecker, S. DeLong, C. Rosa, B. Jones, R. Lamb, A. M. Rosinski, T. P. McCrink, T. E. Dawson, G. Seitz, R. S. Rubin, C. Glennie, D. Hauser, T. Ericksen, D. Mardock, D. F. Hoirup, and J. D. Bray (2014), Key recovery factors for the August 24, 2014, South Napa earthquake, U.S. Geological Survey Open-File Report 2014-1249, doi:10.3133/ofr20141249.

Lagler, K., M. Schindelegger, J. Böhm, H. Krásná, and T. Nilsson (2013), GPT2: Empirical slant delay model for radio space geodetic techniques, Geophys. Res. Lett., 40, 1069–1073, doi:10.1002/grl.50288.

Langenheim, V. E., R. W. Graymer, R. C. Jachens, R. J. McLaughlin, D. L. Wagner, and D. S. Sweetkind (2010), Geophysical framework of the northern San Francisco Bay region, California, Geosphere, 6, 594–620, doi:10.1130/GES00510.1.

Lienkaemper, J. J., J. S. Galehouse, and R. W. Simpson (2001), Long-term monitoring of creep rate along the Hayward Fault and evidence for a lasting creep response to 1989 Loma Prieta earthquake, Geophys. Res. Lett., 28, 2265–2268, doi:10.1029/2000GL012776.

Lienkaemper, J. J., S. B. DeLong, C. J. Domrose, and C. M. Rosa (2016), Afterslip behavior following the 2014 M 6.0 South Napa earthquake with implications for afterslip forecasting on other seismogenic faults, Seismol. Res. Lett., 87, 609–619, doi:10.1785/0220150262.

Lyard, F., F. Lefevre, T. Letellier, and O. Francis (2006), Modelling the global ocean tides: modern insights from FES2004, Ocean Dyn., 56, 394–415, doi:10.1007/s10236-006-0086-x.

Marone, C. J., C. H. Scholz, and R. Bilham (1991), On the mechanics of earthquake afterslip, J. Geophys. Res., 96, 8441–8452, doi:10.1029/91JB00275.

Melgar, D., J. Geng, B. W. Crowell, J. S. Haase, Y. Bock, W. C. Hammond, and R. M. Allen (2015), Seismogeodesy of the 2014 M_w6.1 Napa earthquake, California: Rapid

response and modeling of fast rupture on a dipping strike-slip fault, J. Geophys. Res., 120, 5013–5033, doi:10.1002/2015JB011921.

Morelan, A., C. C. Trexler, and M. E. Oskin (2015), Surface-rupture and slip observations on the day of the 24 August 2014 South Napa earthquake, Seismol. Res. Lett., 86, 1119–1127, doi:10.1785/0220140235.

Petit, G., and B. Luzum (eds.) (2010), IERS Conventions, IERS Technical Note, 36, http://www.iers.org/IERS/EN/Publications/TechnicalNotes/tn36.html.

Reilinger, R., S. McClusky, P. Vernant, S. Lawrence, S. Ergintav, R. Cakmak, H. Ozener, F. Kadirov, I. Guliev, R. Stepanyan, M. Nadariya, G. Hahubia, S. Mahmoud, K. Sakr, A. ArRajehi, D. Paradissis, A. Al-Aydrus, M. Prilepin, T. Guseva, E. Evren, A. Dmitrotsa, S. V. Filikov, F. Gomez, R. Al-Ghazzi, and G. Karam (2006), GPS constraints on continental deformation in the Africa-Arabia-Eurasia continental collision zone and implications for the dynamics of plate interactions, J. Geophys. Res., 111, B05411, doi:10.1029/2005JB004051.

Scholz, C. H. (1998), Earthquakes and friction laws, Nature, 391, 37–42, doi:10.1038/34097.

Stein, R. S. (1999), The role of stress transfer in earthquake occurrence, Nature, 402, 605–609, doi:10.1038/45144.

Toda, S., R. S. Stein, K. Richards-Dinger, and S. Bozkurt (2005), Forecasting the evolution of seismicity in southern California: Animations built on earthquake stress transfer, J. Geophys. Res., 110, B05S16, doi:10.1029/2004JB003415.

Toda, S., R. S. Stein, V. Sevilgen, and J. Lin (2011), Coulomb 3.3 graphic-rich deformation and stress-change software for earthquake, tectonic, and volcano research and teaching—user guide, USGS Open-File Report 2011-1060, http://pubs.usgs.gov/of/2011/1060/.

Wagner, D. L., and E. J. Bortugno (1982), Geologic map of the Santa Rosa quadrangle, California, 1:250,000, ftp://ftp.consrv.ca.gov/pub/dmg/pubs/rgm/RGM_002A/RGM_002A_SantaRosa_1982_Sheet1of5.pdf.

Waldhauser, F. (2009), Near-real-time double-difference event location using long-term seismic archives, with application to northern California, Bull. Seismol. Soc. Amer., 99, 2736–2748, doi:10.1785/0120080294.

Wei, S., S. Barbot, R. Graves, J. J. Lienkaemper, T. Wang, K. Hudnut, Y. Fu, and D. Helmbergeret (2015), The 2014 M_w 6.1 South Napa earthquake: a unilateral rupture with shallow asperity and rapid afterslip, Seismol. Res. Lett., 86, 344–354, doi:10.1785/0220140249.

Wesling, J. R., and K. L. Hanson (2008), Mapping of the West Napa Fault Zone for input into the northern California Quaternary fault database, USGS NEHRP External Award Number 05HQAG0002, http://earthquake.usgs.gov/research/external/reports/05HQAG0002.pdf.

Wright, T. J., J. R. Elliott, H. Wang, and I. Ryder (2013), Earthquake cycle deformation and the Moho: Implications for the rheology of continental lithosphere, Tectonophysics, 609, 504–523, doi:10.1016/j.tecto.2013.07.029.